nature communications

Article

https://doi.org/10.1038/s41467-025-62787-7

Highly selective synthesis of interlocked carbazole-based cages and their applications in photothermal seawater desalination

Received: 26 November 2024

Accepted: 29 July 2025

Published online: 11 August 2025

Check for updates

Ming-Yu Lu[1,2,4], Jian-Xin Yang[1,4], Ya-Ning Xu[3,4], Yin-Hang Chai[1], Xiao-Qian Wan[1], Ying Zhao[1] ✉, Francisco Aznarez[1], Dan Tian[3] ✉, Li-Long Dang[1,2] ✉ & Lu-Fang Ma[1,2]

The design and assembly of interlocked supramolecular cages is of interest due to their exquisite topological configuration and excellent performance in a variety of applications. We introduce two carbazole-based ligands **L1** and **L2**, they combine with four distinct half-sandwich rhodium building blocks to form three molecular-tweezer-like compounds, three interlocked cages, tetranuclear macrocycle, and hexanuclear cage. Stacking interactions between carbazole groups facilitate the formation of interlocked structures. Single-crystal X-ray diffraction, Nuclear Magnetic Resonance Spectroscopy and Electrospray Ionization Mass Spectrometry determine their structures. The compounds **5**$(OTf)_{12}$, **6**$(OTf)_{12}$ and **7**$(OTf)_{12}$ exhibit broad-band absorption from Ultraviolet-Visible Spectroscopy to the Near-Infrared regions and remarkable photothermal conversion. They are incorporated into membranes **5′**$(OTf)_{12}$, **6′**$(OTf)_{12}$, and **7′**$(OTf)_{12}$, whose applications in solar energy-driven steam generation are studied. Evaporation rates of 0.77, 1.52, and 1.37 $kg{\cdot}m^{-2}{\cdot}h^{-1}$ are recorded for **5′**$(OTf)_{12}$, **6′**$(OTf)_{12}$, and **7′**$(OTf)_{12}$, respectively, indicating their suitability to collect fresh water from desalination and wastewater treatment.

The synthesis and application of intricate interlocked supramolecular compounds has attracted increasing attention during the past decades[1–3]. Significant contributions to this field have been done by Stoddart[4], Sauvage[5], Fujita[6], Stang[7,8], Nitschke[9], Jin[10,11], and others. Various sophisticated interlocked structures have been obtained by coordination driven self-assembly or metal-ion templated strategies, including [2, 3, 4, 5]catenanes[12–15], 5-fold interlocked [2]catenanes[16], interlocking two trefoil knots[17,18], and triply interlocked [2]catenanes[19–22]. Their application in photothermal conversion[23], catalysis[24], and polymer weaving[25], has been studied. Moreover, structural transformation strategies have also been explored, and various structural conversions of these intricate compounds were described. Thus, reversibly structural transformation between double trefoil (3_1) and figure-eight knot (4_1) was achieved by introducing/removing potassium ions[17]. Topological transformation between a D-shaped binuclear metallacycle and a molecular Borromean ring was observed via controlled oxidation of thioethers[26]. Recently, the conversion between a trefoil knot and a Solomon link was achieved via Diels-Alder click reaction[27]. These studies enabled the synthesis and isolation of compounds that were previously difficult or impossible to form.

Interlocked cages are very rare topological species[28–30]. While the transformation between interlocked cages and single cages has been reported[31], research on the conversion into other chemical species is infrequent, as well as application studies.

[1]College of Chemistry and Chemical Engineering, Luoyang Normal University, Luoyang, PR China. [2]College of Chemistry, Zhengzhou University, Zhengzhou, PR China. [3]Co-Innovation Center of Efficient Processing and Utilization of Forest Resources, College of Materials Science and Engineering, Nanjing Forestry University, Nanjing, PR China. [4]These authors contributed equally: Ming-Yu Lu, Jian-Xin Yang, Ya-Ning Xu.
✉e-mail: zhaoyingchem@126.com; tiandan@njfu.edu.cn; 16110220019@fudan.edu.cn

Previous research has shown that interlocked supramolecular structures based on half-sandwich rhodium and iridium building blocks exhibit significant synthetic advantages, such as directional coordination, strong crystallinity, and good solubility in a variety of solvents. In addition, they also display remarkable photoquenching characteristics. Note that π···π stacking interactions promote the enhancement of UV visible absorption and photothermal conversion performance. And interlocked structures are formed based on the stacking of large π-conjugated molecules.

In recent years, catenanes[32–34], knots[35,36], ravels[37], and interlocked cages[38,39] based on half-sandwich rhodium and iridium building blocks were rationally designed and isolated. Some of these interlocked supramolecular structures exhibited significant photothermal conversion properties, which could be attributed to the free radical effect of the half-sandwich units. It is assumed that π···π stacking interactions in the compounds hamper the radiative and promote the non-radiative transition process, thereby enhancing photothermal conversion performance. Solar-driven desalination represents a promising approach to alleviate global water scarcity by utilizing photothermal conversion to transform solar energy into heat for water evaporation. Ideal photothermal materials must exhibit broad spectral absorption and high energy conversion efficiency. Current research has explored diverse candidates, such as carbon-based nanomaterials[40], metal oxides[41], covalent organic frameworks (COFs)[42], and coordination polymers[43]. Nevertheless, the development of interlocked coordination supramolecular possessing highly conjugated effect and enhanced photothermal performance remains a critical challenge because of their synthetic complexity. We hypothesize that the good photothermal conversion properties and the proven water stability of half-sandwich based interlocked compounds are useful features for application in seawater desalination. Besides, the excellent solubility in organic solvents and good crystallinity of these structures allows it to be recycled as a desalination material, showing its uniqueness compared to other materials. Thus, selecting suitable half-sandwich based building units to synthesize multi-interlocked topological structures will show unique advantages in photothermal seawater desalination field.

Carbazole is a molecule endowed with large π-conjugated planes that are, in principle, suitable to form stable π···π stacking interactions, useful for the formation of interlocked supramolecular structures. Taking this information into consideration, two carbazole-based bidentate and tridentate ligand precursors (**L1** and **L2**) were prepared and used in this study. Thus, compounds **L1** and **L2** were mixed with a series of suitable Cp*Rh (Cp* = pentamethylcyclopentadienyl) based building blocks, **E1**$(OTf)_2$, **E2**$(OTf)_2$, **E3**$(OTf)_2$, and **E4**$(OTf)_2$, in an attempt to obtain half-sandwich-based interlocked supramolecular compounds of different sizes. Our research indicated that the dimensions and chemical properties of the building blocks are a key factor for the formation of stable, intricate structures. Thus, the metal-metal non-bonding distance between building blocks must be ~7.5 Å to yield π···π stacking interactions. Three molecular-tweezer-like compounds **1**$(OTf)_8$, **2**$(OTf)_8$, and **3**$(OTf)_8$, a tetranuclear macrocycle **4**$(OTf)_4$, three interlocked cages **5**$(OTf)_{12}$, **6**$(OTf)_{12}$, and **7**$(OTf)_{12}$, and a hexanuclear cage **8**$(OTf)_6$ were obtained and fully characterized by single crystal X-ray diffraction analysis, NMR spectroscopy, and ESI-TOF-MS analysis. Remarkably, π···π stacking interactions were observed in the isolated interlocked molecular-tweezer-like compounds **1**$(OTf)_8$, **2**$(OTf)_8$, and **3**$(OTf)_8$, as well as in the interlocked molecular cages, promoting different NIR photothermal conversion effects. Due to the exceptional photothermal conversion capability exhibited by **5**$(OTf)_{12}$, **6**$(OTf)_{12}$, and **7**$(OTf)_{12}$, we used them to prepare the membranes **5′**$(OTf)_{12}$, **6′**$(OTf)_{12}$, and **7′**$(OTf)_{12}$ by adding interlocked cages **5**$(OTf)_{12}$, **6**$(OTf)_{12}$, and **7**$(OTf)_{12}$ to a microcellular substrate without any additives, subsequently, the performance in solar steam generation was tested. The recorded evaporation rate of membranes **5′**$(OTf)_{12}$, **6′**$(OTf)_{12}$, and **7′**$(OTf)_{12}$ reached 0.77, 1.52, and 1.37 $kg\,m^{-2}\,h^{-1}$, which indicates a favorable ability to collecting fresh water by desalination and wastewater treatment.

Results

Self-assembly of molecular-tweezer-like compounds 1$(OTf)_8$, 2$(OTf)_8$ and 3$(OTf)_8$, and tetranuclear macrocycle 4$(OTf)_4$

Mixture of building blocks **E1**$(OTf)_2$, **E2**$(OTf)_2$, or **E3**$(OTf)_2$ with ligand precursor **L1** yielded three molecular-tweezer-like compounds **1**$(OTf)_8$, **2**$(OTf)_8$ or **3**$(OTf)_8$, respectively in 87.4%, 86.7% and 87.2% yields. The self-assembly of building block **E4**$(OTf)_2$ with **L1** resulted in the isolation of tetranuclear macrocycle **4**$(OTf)_4$. Slow diffusion of isopropyl ether into a concentrated methanolic solutions of these compounds led to the formation of single crystals of **1**$(OTf)_8$, **2**$(OTf)_8$, **3**$(OTf)_8$, and **4**$(OTf)_4$ suitable for an X-ray diffraction analysis (Fig. 1).

Single-crystal X-ray diffraction studies unambiguously confirmed the molecular structure of tweezer-like compounds **1**$(OTf)_8$, **2**$(OTf)_8$, and **3**$(OTf)_8$. They belong to the *P*21/*c*, *P*-1, and *P*21/*n* space groups, respectively. The molecular structure of both compounds, **1**$(OTf)_8$, **2**$(OTf)_8$, and **3**$(OTf)_8$, exhibited two half-sandwich rhodium building units connected to two pyridine ligands **L1**, thereby forming a "boat-shaped" tetranuclear macrocyclic compound (Supplementary Figs. 11b, c). A large inner cavity was observed, with the shorted measured distance between two **L1** ligands of 6.67 Å. Two identical tetranuclear macrocycles coexisted a clamped manner and built a stable octanuclear assembly. Compound **2**$(OTf)_8$ exhibited slightly twisted π···π stacking interactions with interlayer distances of 3.39, 3.49, and 3.45 Å (Fig. 2a, b, e). Similarly, compound **3**$(OTf)_8$ also showed π···π stacking interactions featuring interlayer distances of 3.43, 3.38, and 3.42 Å (Fig. 2c, d). The unique structural features of these molecular-tweezer-like compounds provide highly valuable reference parameters for future molecular design. Compounds **2**$(OTf)_8$ and **3**$(OTf)_8$ were also characterized by ^{1}H NMR, ^{1}H-^{1}H COSY NMR, and ^{1}H DOSY NMR spectrum. As expected, the relatively small cavity size would hamper the generation of a complicated molecular structure. Thus, the combination of building block **E4**$(OTf)_2$ (metal-to-metal distance of 5.80 Å) and ligand precursor **L1** led to a simple tetranuclear macrocyclic structure, which was identified by NMR spectroscopy (Supplementary Figs. 23, 24 and 25) and mass spectrometry (Supplementary Figs. 54a, 55d and 56g).

Self-assembly of interlocked cages 5$(OTf)_{12}$, 6$(OTf)_{12}$ and 7$(OTf)_{12}$, and hexanuclear cage 8$(OTf)_6$

The self-assembly of ligand precursor **L2** with building blocks **E1**$(OTf)_2$, **E2**$(OTf)_2$, and **E3**$(OTf)_2$ was next investigated. We hypothesized that the use of a tridentate ligand precursor instead of **L1**, but endowed with similar π-conjugated properties, could contribute towards formation of interlocked cages instead of molecular-tweezer-like structures. Reaction of the building blocks **E1**$(OTf)_2$, **E2**$(OTf)_2$, or **E3**$(OTf)_2$ with **L2** led to the formation of interlocked cages **5**$(OTf)_{12}$ (light yellow), **6**$(OTf)_{12}$ (brown), or **7**$(OTf)_{12}$ (green), respectively, in 87.5%, 89.1% or 86.5% yield. The self-assembly of building block **E4**$(OTf)_2$ with **L1** resulted in the construction of hexanuclear cage **8**$(OTf)_6$, which was identified by NMR spectroscopy and mass spectrometry. Slow diffusion of isopropyl ether into saturated solutions of **5**$(OTf)_{12}$, **6**$(OTf)_{12}$, and **7**$(OTf)_{12}$ in methanol yielded single crystals suitable for an X-ray diffraction analysis (Fig. 1).

Single-crystal X-ray diffraction analysis of **5**$(OTf)_{12}$, **6**$(OTf)_{12}$, and **7**$(OTf)_{12}$ confirmed their architectures (Supplementary Figs. 12b, c). The molecular structures of compounds **5**$(OTf)_{12}$, **6**$(OTf)_{12}$, and **7**$(OTf)_{12}$ were categorized into the *P*21/*n*, *P*21/*c*, and *Pc* spatial groups, respectively. The molecular structure of compound **5**$(OTf)_{12}$ showed each rhodium ion of building block **E1**$(OTf)_2$ coordinating one pyridine nitrogen atom of the carbazole-based ligand **L2**. Three building units **E1**$(OTf)_2$ formed a self-assembly with two ligands **L2** in a coplanar spatial arrangement, thereby yielding a hexanuclear **L_2E_3**$(OTf)_6$

https://doi.org/10.1038/s41467-025-62787-7

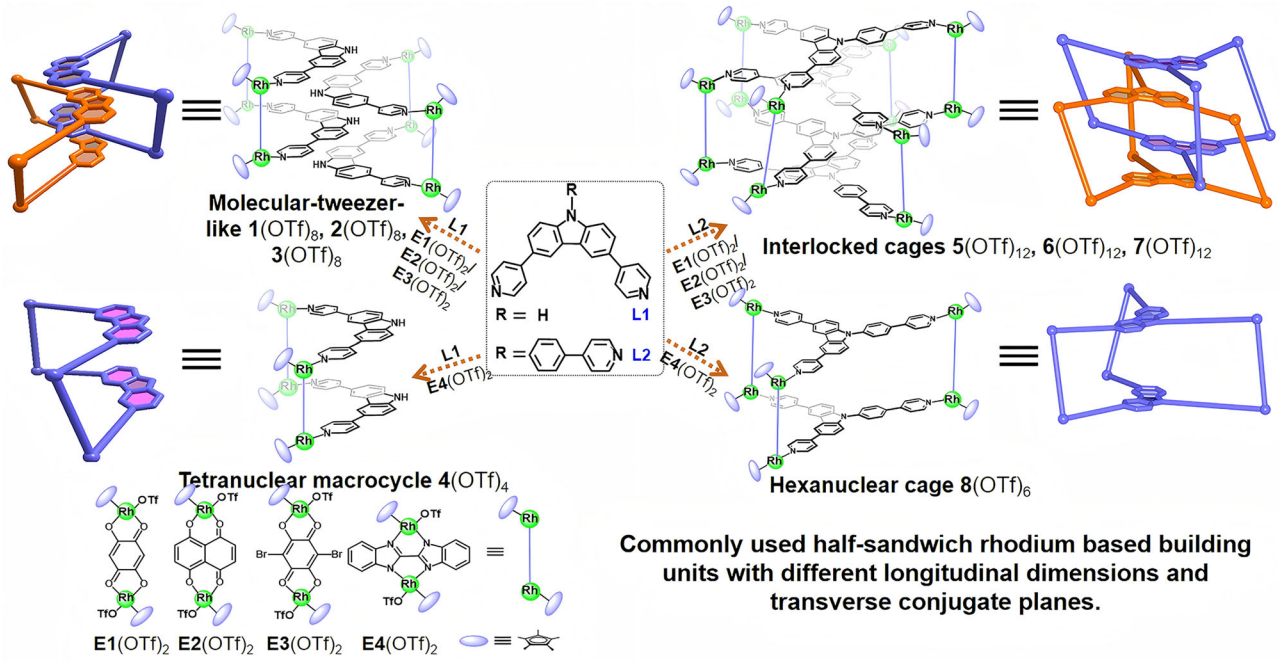

Fig. 1 | Synthesis of compounds 1(OTf)$_8$, 2(OTf)$_8$, 3(OTf)$_8$, 4(OTf)$_4$, 5(OTf)$_{12}$, 6(OTf)$_{12}$, 7(OTf)$_{12}$ and 8(OTf)$_6$. Synthesis of molecular-tweezer-like compounds **1**(OTf)$_8$, **2**(OTf)$_8$ and **3**(OTf)$_8$, tetranuclear macrocycle **4**(OTf)$_4$, interlocked cages **5**(OTf)$_{12}$, **6**(OTf)$_{12}$ and **7**(OTf)$_{12}$, and Hexanuclear cage **8**(OTf)$_6$.

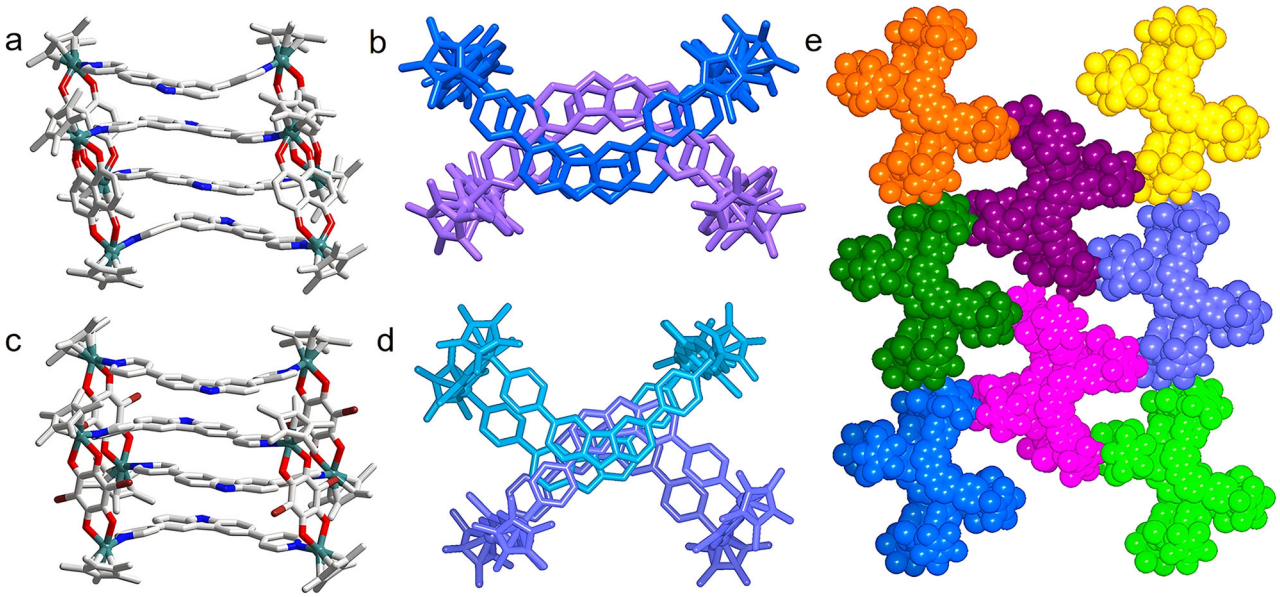

Fig. 2 | Molecular structures of molecular-tweezer-like compounds 2(OTf)$_8$ and 3(OTf)$_8$. a, **c** side view and representation showing π···π stacking interactions between carbazole units; **b**, **d** top view and **e** space-filling representations. Most hydrogen atoms, anions, and solvent molecules have been omitted for clarity (N blue, O red, C gray, Rh aqua, Br dark red).

"propeller-shaped" cage. Two identical **L$_2$E$_3$**(OTf)$_6$ cages appeared in an interlocked fashion, resulting in a dodecanuclear topological configuration (Fig. 3a–c). The two intricately intertwined triangular prisms featured the carbazole facet of the counterpart occupying the interior remaining space. A set of quadruple π···π stacking interactions could be observed by the parallel alignment of aromatic rings in the molecular structure, resulting in a substantial stabilization of the structural configuration. The measured interlayer distances are 3.25, 3.78, and 3.51 Å, typical of π···π stacking interactions. Similarly, π···π stacking interactions could also be clearly observed in the molecular structure of compound **6**(OTf)$_{12}$, featuring interlayer distances of 3.45, 3.51, and 3.31 Å (Fig. 3d–f).

Subsequently, NMR spectroscopy studies were performed in CD_3OD. The ^{1}H NMR spectrum of **1**(OTf)$_8$ (Supplementary Fig. 14) exhibited two similar doublets at 8.09 and 7.51 ppm, respectively, which were assigned to the protons of the pyridinyl groups of **L1**. Furthermore, two sets of signals at 7.18 and 6.78 ppm were assigned to protons of carbazole groups, as well as the two singlets observed at 7.06 and 6.70 ppm. The signal corresponding to the benzoquinone proton of the building block **E1**(OTf)$_2$ appeared at 5.97 ppm. The resonance corresponding to the protons of the Cp* group of ligand **L1** appeared at 1.84 ppm. Using a combination of ^{1}H-^{1}H COSY NMR and ^{1}H DOSY NMR spectra ($D = 2.59 \times 10^{-6}$ cm^2 s^{-1}) (Supplementary Figs. 15 and 16), additional signals could be unambiguously assigned,

https://doi.org/10.1038/s41467-025-62787-7

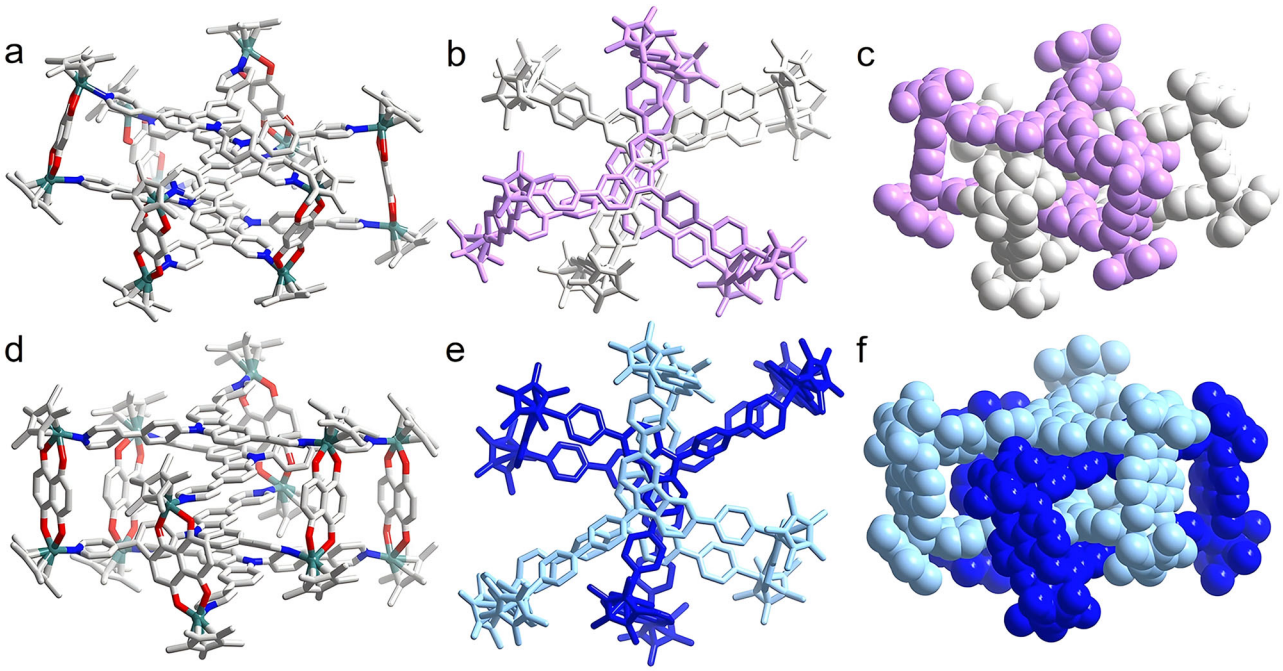

Fig. 3 | Molecular structures of interlocked cages 5(OTf)$_{12}$ and 6(OTf)$_{12}$. **a**, **d** side view and representation showing π···π stacking interactions between carbazole units; **b**, **e** top view; **c**, **f** space-filling representations. Most hydrogen atoms, anions, and solvent molecules have been omitted for clarity (N blue, O red, C gray, Rh aqua).

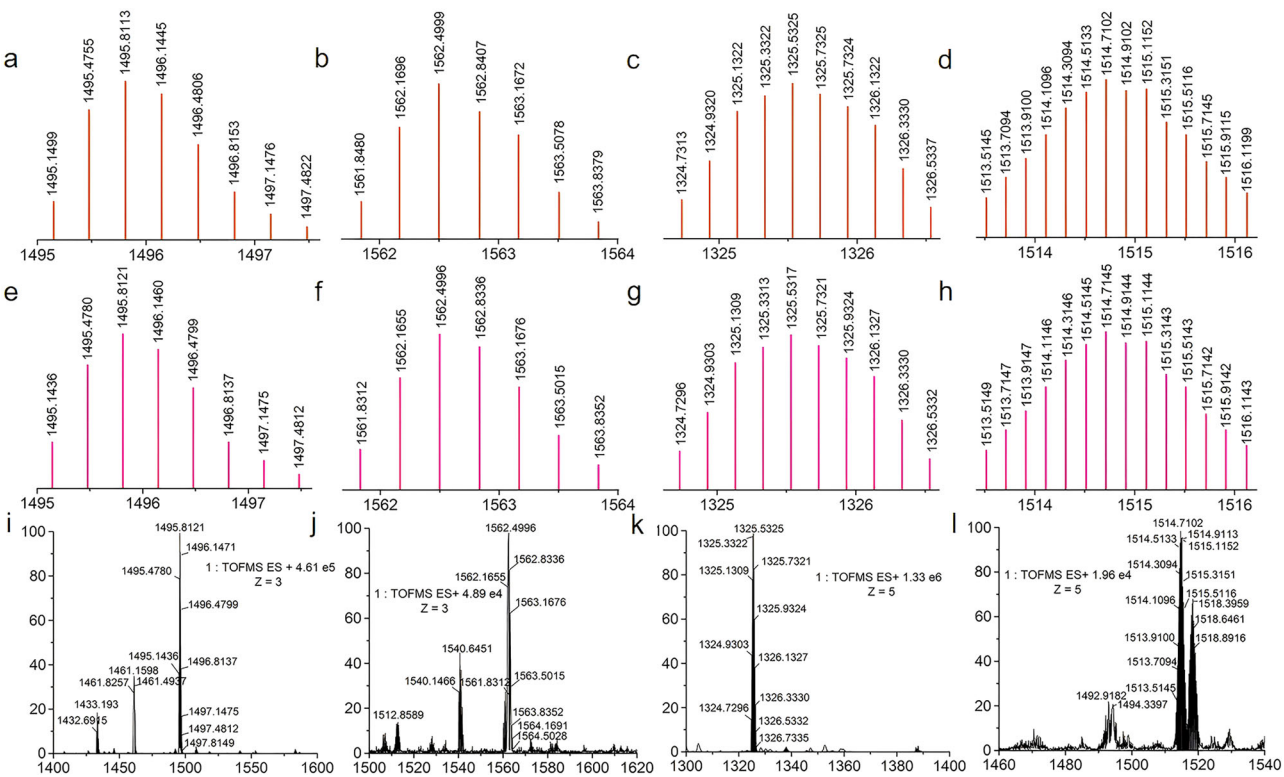

Fig. 4 | ESI-TOF-MS experiment of compounds 1(OTf)$_8$, 2(OTf)$_8$, 5(OTf)$_{12}$, and 7(OTf)$_{12}$. ESI-TOF-MS spectra of (**a**, **e**, **i**) [**1**(OTf)$_8$-3OTf$^-$]$^{3+}$; **b**, **f**, **j** [**2**(OTf)$_8$-3OTf$^-$]$^{3+}$; **c**, **g**, **k** [**5**(OTf)$_{12}$-5OTf$^-$]$^{5+}$ and **d**, **h**, **l** [**7**(OTf)$_{12}$-5OTf$^-$]$^{5+}$.

indicating the potential formation of an intricate interlocked tweezer-like structure. In addition, ESI-TOF-MS spectrum of **1**(OTf)$_8$ displayed a strong peak at m/z = 1495.81 ([**1**(OTf)$_8$-3OTf$^-$]$^{3+}$) (Fig. 4a, e, i). Similarly, the proposed structure of compounds **2**(OTf)$_8$ ($D = 2.65 \times 10^{-6}$ cm^2 s^{-1}) (Supplementary Figs. 17, 18 and 19) and ^{3}(OTf)$_8$ ($D = 2.49 \times 10^{-6}$ cm^2 s^{-1}) (Supplementary Figs. 20, 21 and 22) was also supported by ^{1}H NMR, ^{1}H-^{1}H COSY NMR, and ^{1}H DOSY NMR spectroscopy. Furthermore, the ESI-TOF-MS spectrum of **2**(OTf)$_8$ displayed a strong peak at m/z = 1562.49 ([**2**(OTf)$_8$-3OTf$^-$]$^{3+}$) (Figs. 4b, f, j). In the ^{1}H NMR spectrum of **7**(OTf)$_{12}$ (Fig. 5b), six singlets appeared at chemical shifts 1.94, 1.87, 1.84, 1.76, 1.70, and 1.58 ppm, which were assigned to the protons of the Cp* group of compound **7**(OTf)$_{12}$. Additionally, three resonance

https://doi.org/10.1038/s41467-025-62787-7

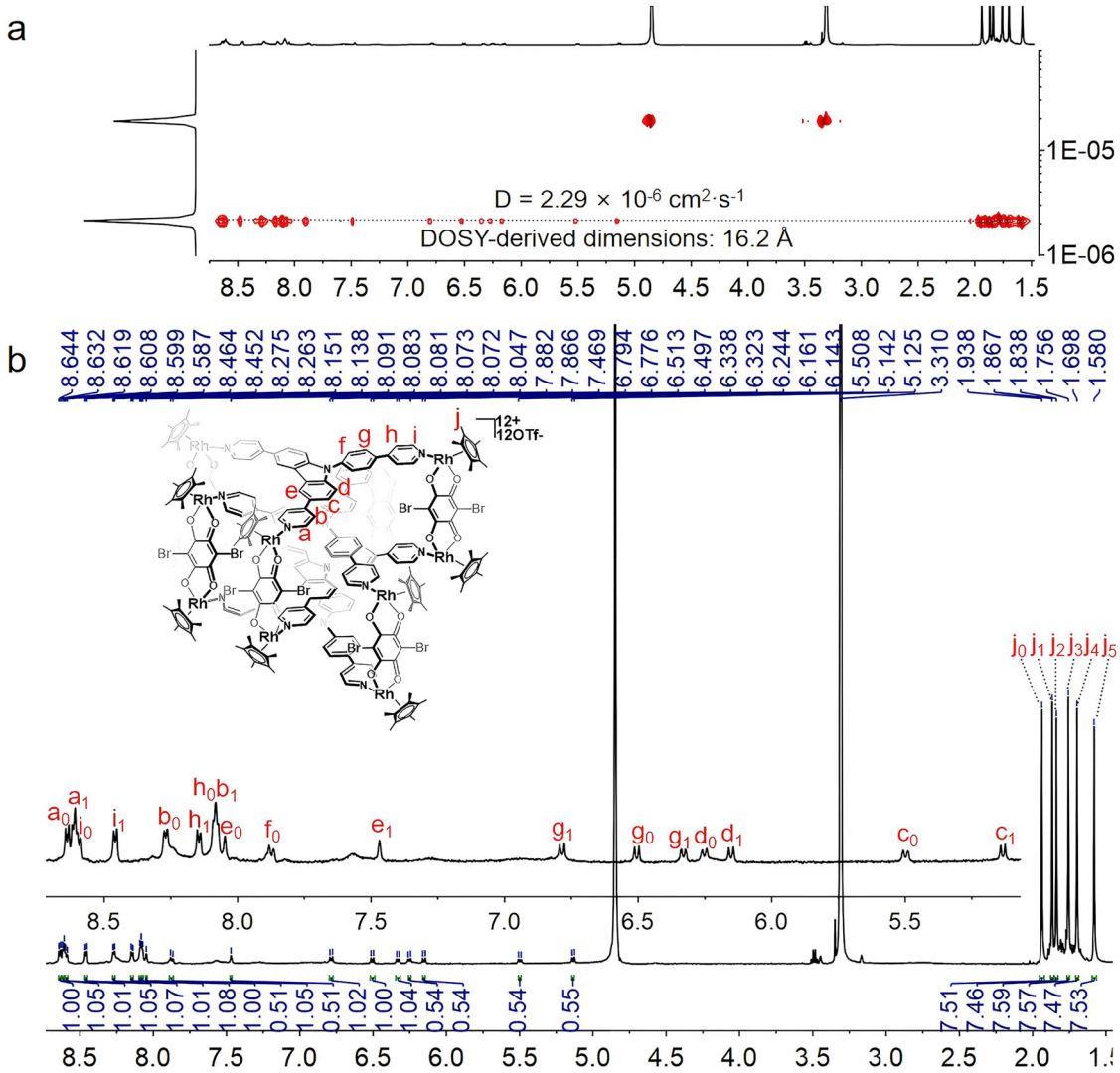

Fig. 5 | NMR experiment of compound 7(OTf)$_{12}$. **a** ^{1}H DOSY NMR spectrum (500 MHz, CD_3OD, ppm) of interlocked cage **7**$(OTf)_{12}$ (2.29×10^{-6} cm^2 s^{-1}) (19.5 mM, with respect to Cp*Rh); **b** ^{1}H NMR spectrum (500 MHz, CD_3OD, ppm) of interlocked cage **7**$(OTf)_{12}$ (19.5 mM, with respect to Cp*Rh).

sets belonged to pyridine proton signals (8.64, 8.62, 8.60, 8.28, 8.09, 8.08 ppm), as well as the multiplets at 8.46 and 8.15 ppm. The protons of the carbazole groups displayed resonances at 8.05, 7.47, 6.26, 6.14, 5.51, and 5.14 ppm. The structure of compound **7**$(OTf)_{12}$ was also supported by ^{1}H-^{1}H COSY NMR (Supplementary Fig. 33) and ^{1}H DOSY NMR spectra ($D = 2.29 \times 10^{-6}$ cm^2 s^{-1}) (Fig. 5a). Interestingly, the ESI-TOF-MS spectrum of **7**$(OTf)_{12}$ exhibited a strong peak at m/z = 1514.71 ([**7**$(OTf)_{12}$-5OTf$^-$]$^{5+}$) (Fig. 4d, h, i). The experimental ESI-TOF-MS measurement was in good agreement with its corresponding theoretical distribution, thereby indicating the existence of a dodecanuclear organometallic interlocked cage in solution. Similarly, the proposed structure of compound **5**$(OTf)_{12}$ ($D = 2.33 \times 10^{-6}$ cm^2 s^{-1}) (Supplementary Figs. 26–29) was supported by the recorded ^{1}H NMR, ^{1}H-^{1}H COSY NMR, and ^{1}H DOSY NMR spectra. In addition, ESI-TOF-MS spectrum of **5**$(OTf)_{12}$ displayed a remarkable peak at m/z = 1325.53 ([**5**$(OTf)_{12}$-5OTf$^-$]$^{5+}$) (Fig. 4c, g, k).

Subsequently, the ^{1}H NMR, ^{1}H-^{1}H COSY NMR and ^{1}H DOSY NMR ($D = 2.31 \times 10^{-6}$ cm^2 s^{-1}) spectra of compound **6**$(OTf)_{12}$ were also recorded (Supplementary Figs. 30, 31 and 32). The ^{1}H NMR spectrum of **6**$(OTf)_{12}$ revealed six singlets at chemical shifts 1.83, 1.77, 1.75, 1.64, 1.60, and 1.37 ppm, which were assigned to the protons of the Cp* groups. Additionally, the ESI-TOF-MS spectrum of **6**$(OTf)_{12}$ exhibited a prominent peak at m/z = 2408.55, corresponding to the [**6**$(OTf)_{12}$-3OTf$^-$]$^{3+}$ ion (Supplementary Fig. 54b, e, and h). Next, we decided to study the effect of varying the concentration and different polar solvent of compound **6**$(OTf)_{12}$ on its structural features. Thus, no significant alterations were observed in the ^{1}H NMR spectra of **6**$(OTf)_{12}$ (500 MHz, CD_3OD, ppm) upon increasing its concentration in CD_3OD from 1 eq. to 5 eq. (Supplementary Fig. 37). In addition, The ^{1}H NMR of **6**$(OTf)_{12}$ has been tested in CD_3CN (Supplementary Fig. 38). The ^{1}H NMR spectrum displayed a clear set of proton signals and successfully assign the signals of **6**$(OTf)_{12}$ through ^{1}H-^{1}H COSY spectrum (Supplementary Fig. 39). The ^{1}H DOSY spectrum revealed a single diffusion coefficient, indicating that only one stoichiometry exists in solution (Supplementary Fig. 40). Therefore, compound **6**$(OTf)_{12}$ exhibits remarkable structural stability in solution. Moreover, The ^{1}H-^{1}H NOESY spectroscopy of **5**$(OTf)_{12}$, **6**$(OTf)_{12}$, and **7**$(OTf)_{12}$ has been tested to confirm the spatial relationship of the interlocked structure (Supplementary Figs. 44, 45 and 46).

In an effort to shed light on the role played by the size of the half-sandwich-based building blocks in the formation of the described interlocked supramolecular compounds, the Cp*Rh building unit **E4**$(OTf)_2$ was prepared. Compound **8**$(OTf)_6$ was formed by mixing **L2** and **E4**$(OTf)_2$, and has been isolated in a good yield of 87.8% as a yellow solid. The ^{1}H NMR spectrum of **8**$(OTf)_6$ showed a significant number of resonances, which were unambiguously assigned to protons with the

https://doi.org/10.1038/s41467-025-62787-7

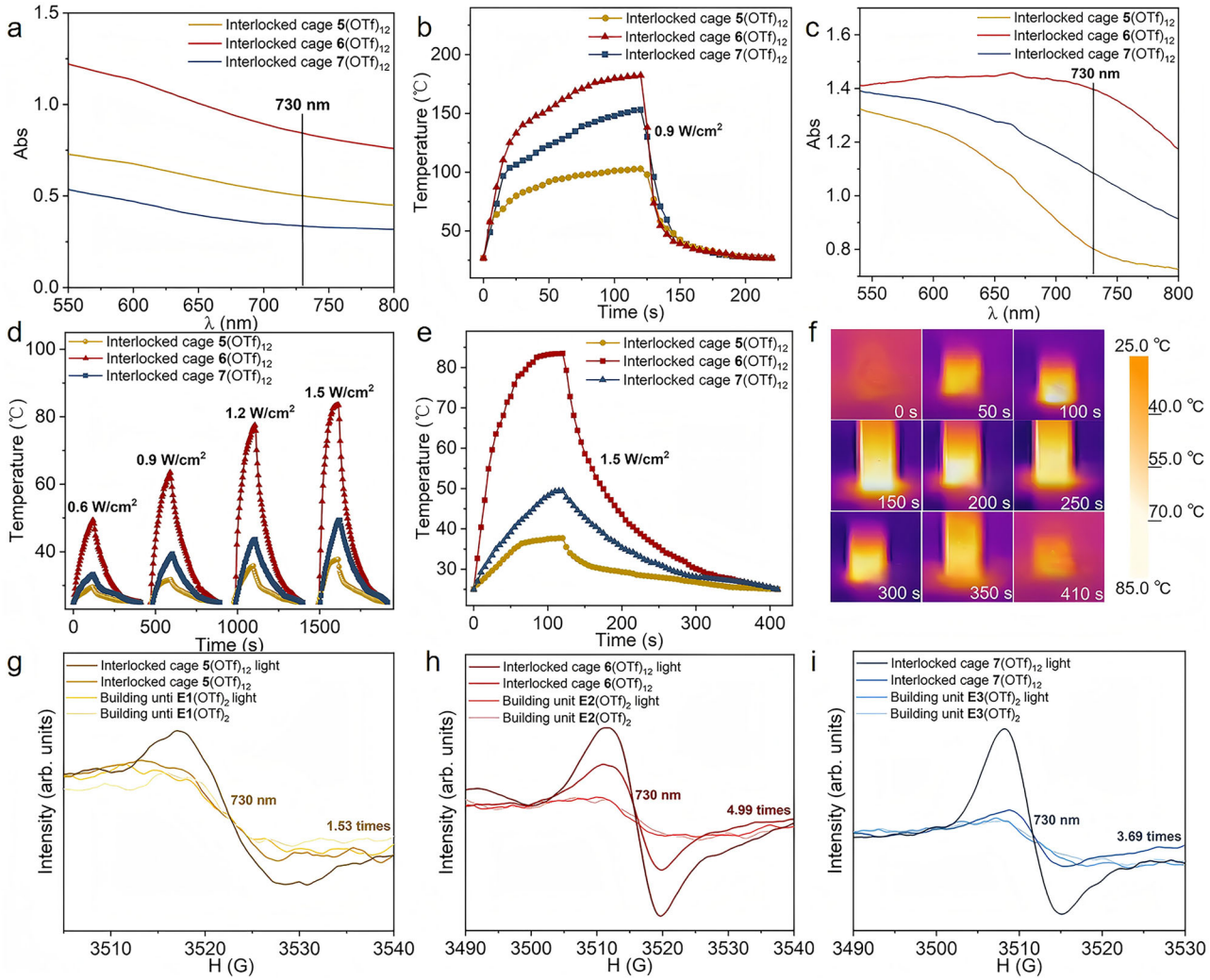

Fig. 6 | UV-Vis, NIR photothermal conversion and EPR experiments. UV-Vis absorption of compounds **5**$(OTf)_{12}$, **6**$(OTf)_{12}$ and **7**$(OTf)_{12}$ at **a** 550–800 nm in CH_3OH and **c** 540–800 nm in solid; NIR photothermal conversion curves of **5**$(OTf)_{12}$, **6**$(OTf)_{12}$ and **7**$(OTf)_{12}$ at **b** 0.6 W/cm^2 in solid and **e** 1.5 W/cm^2 in CH_3OH; **d** NIR photothermal conversion curves of **5**$(OTf)_{12}$, **6**$(OTf)_{12}$ and **7**$(OTf)_{12}$ at 0.6, 0.9, 1.2, and 1.5 W/cm^2; **f** NIR thermal images of **6**$(OTf)_{12}$ in the spectrophotometer cell; **g**, **h** and **i** EPR spectra of compounds **5**$(OTf)_{12}$, **6**$(OTf)_{12}$ and **7**$(OTf)_{12}$ (100 Hz, 298 K).

assistance of ^{1}H-^{1}H COSY NMR and ^{1}H DOSY NMR spectra ($D = 2.69 \times 10^{-6}$ cm^2 s^{-1}) (Supplementary Figs. 34, 35 and 36). Thus, the ^{1}H NMR spectrum of **8**$(OTf)_6$ showed sets of doublets at 8.24, 8.16, 7.72 and 7.61 ppm, which belonged to the protons of the pyridinyl groups of ligand **L1**. Furthermore, the sets signals at 7.23 and 7.11 ppm were attributed to the protons of the carbazole groups. While the resonances belonging to the protons of the BiBzIm moiety appeared as two signals at 8.02 and 7.71 ppm, the signal at 1.93 ppm was attributed to the Cp* protons. Moreover, The ESI-TOF-MS spectrum of **8**$(OTf)_6$ displayed a significant peak at m/z = 1173.86, which was attributed to the [**8**$(OTf)_6$-3OTf]$^{3+}$ ion (Supplementary Figs. 54c, 54f, and 54i).

Near-infrared (NIR) photothermal conversion studies

Recent studies concerning the application of half-sandwich rhodium (III) supramolecular assemblies have highlighted the importance of π···π stacking interactions to preserve the structure. In addition, the presence of half-sandwich metal fragments within the assemblies delivers a useful light quenching phenomenon, which significantly hampers radiative transition processes while promoting non-radiative energy transfers. This synergistic effect ultimately allows the achievement of highly efficient NIR photothermal conversions[44]. We thereafter investigated the NIR photothermal conversion ability of organometallic interlocked cages **5**$(OTf)_{12}$, **6**$(OTf)_{12}$, and **7**$(OTf)_{12}$. Note that their structure exhibits similarities, while the size varies. The selected molar ratio of compounds **5**$(OTf)_{12}$, **6**$(OTf)_{12}$, and **7**$(OTf)_{12}$ for the experiments has been 1: 1: 1, in order to reach the same stacking quantity. The NIR absorption properties of the compounds at different wavelengths were initially evaluated. Thus, their ultraviolet-visible (UV-vis) spectra within a wavelength range from 200 to 1000 nm were acquired at a compound concentration level of 0.5 mM. Recorded NIR absorption values of compounds **5**$(OTf)_{12}$, **6**$(OTf)_{12}$, and **7**$(OTf)_{12}$ at 730 nm were 0.503, 0.843, and 0.336 (Fig. 6a).

Thus, subsequent photothermal conversion experiments were conducted under laser irradiation at a wavelength of 730 nm. We first conducted measurements of photothermal conversion by using the compounds in solid state as a benchmark, and it was observed that compound **6**$(OTf)_{12}$ exhibited a significantly superior photothermal conversion effect than compounds **5**$(OTf)_{12}$ and **7**$(OTf)_{12}$ (Fig. 6b, c). Compound **6**$(OTf)_{12}$ showed a temperature increase of 155.4 °C (from 26.9 °C to 182.3 °C) at an irradiation intensity of 0.9 W/cm^2 (Supplementary Fig. 60). Thereafter, solutions of the three compounds **5**$(OTf)_{12}$, **6**$(OTf)_{12}$, and **7**$(OTf)_{12}$ underwent photothermal testing at intensities of 1.5 W/cm^2, 1.2 W/cm^2, 0.9 W/cm^2, and 0.6 W/cm^2 (Fig. 6d, e, f), and the recorded results were used to determine the

photothermal conversion efficiencies (Supplementary Figs. 75, 76 and 77). While the temperature of a methanolic solution of **6**$(OTf)_{12}$ increased substantially (from 28.7 °C to 82.8 °C) under a laser irradiation of 1.5 W/cm² at a wavelength of 730 nm (Supplementary Fig. 68), the temperature change associated with a solution of **5**$(OTf)_{12}$ in CH_3OH (from 25.0 °C to 37.7 °C) (Supplementary Fig. 67) and **7**$(OTf)_{12}$ (from 25.0 °C to 49.4 °C) (Supplementary Fig. 69) under the same test conditions were relatively smaller.

Seawater desalination experiment

Photothermal materials are emerging as versatile platforms for applications in photothermal therapy (PTT), catalysis, sensing, and drug delivery[45–48]. Furthermore, the interlocking cages boast excellent structural precision and photothermal conversion efficiency, making them applicable in more areas. The discrepancies observed in the photothermal conversion properties of the three compounds **5**$(OTf)_{12}$, **6**$(OTf)_{12}$, and **7**$(OTf)_{12}$ may be explained by differences in their respective half-sandwich rhodium-based building units. Thus, the electron paramagnetic resonance (EPR) spectra of building units **E1**$(OTf)_2$, **E2**$(OTf)_2$, and **E3**$(OTf)_2$, and compounds **5**$(OTf)_{12}$, **6**$(OTf)_{12}$, and **7**$(OTf)_{12}$ were measured. The robust signals recorded are indicative of the presence of unpaired electrons, which aligns with the charge-transfer interaction observed in the ground state. Note that the intensity of the signals corresponding to the compounds **5**$(OTf)_{12}$, **6**$(OTf)_{12}$, and **7**$(OTf)_{12}$ increased 1.53, 4.99, and 3.69 times in comparison to that of the building units **E1**$(OTf)_2$, **E2**$(OTf)_2$, and **E3**$(OTf)_2$ (Fig. 6g–i). This experimental result may be attributed to the fact that π···π stacking interactions in interlocked cages **5**$(OTf)_{12}$, **6**$(OTf)_{12}$, and **7**$(OTf)_{12}$ promote non-radiative transitions and suppress radiative transitions, leading to an increase in the intensity of EPR signals. Futhermore, the energy levels of building units **E1**$(OTf)_2$, **E2**$(OTf)_2$, and **E3**$(OTf)_2$ have been calculated so that the difference in the photothermal conversion efficiency of interlocked cages can be explored clearly. As shown in Supplementary Fig. 82a, b, c, the building units **E1**$(OTf)_2$ exhibit a larger bandgap, which translates to a higher energy requirement for electrons to transition from the valence band to the conduction band. Certainly, the building units **E2**$(OTf)_2$ exhibits the smallest bandgap; thus, compound **6**$(OTf)_2$ has the best photothermal conversion efficiency.

The lack and decrease of available freshwater resources is a serious issue and has become a global matter of concern. Desalination of seawater represents a suitable solution to this question[49–51]. Owing to the fact that compounds **5**$(OTf)_{12}$, **6**$(OTf)_{12}$, and **7**$(OTf)_{12}$ exhibited remarkable photothermal conversion performance (Supplementary Table 8), we decided to test them in the preparation of membranes desalination processes. A sample of **6**$(OTf)_{12}$ (0.01 mmol) was dispersed in 20 ml of deionized water by sonication for approximately 10 min. Then the membrane **6′**$(OTf)_{12}$ was obtained by vacuum filtration over hydrophilic cellulose film, followed by curing at ambient temperature. Subsequently, membrane **6′**$(OTf)_{12}$ was placed on the top surface of a commercial polystyrene (PS) foam. The entire structure was embedded in the mouth of a quartz vessel, and a hydrophilic non-woven fabric strip was used to link bulk water and membrane **6′**$(OTf)_{12}$ by passing through the center of the PS foam during water delivery. Measurements of steam generation promoted by solar energy were carried out with light intensity of 1 kW m^{-2} using a sunlight simulator with the full solar light spectrum. All the photothermal conversion experiments summarized in this work were conducted under AM 1.5 G, and the mass change has been measured with an electronic balance connected to a computer. The area of the membrane **6′**$(OTf)_{12}$ used for steam generation has been 3.14 cm^2. The temperature of the membrane and the infrared images have been recorded by using an infrared thermal imaging camera. The solar-to-vapor conversion efficiency (%) was evaluated with the following Eq. (1):

$$\eta = \frac{m \times h_{lv}}{C_{opt} \times q_i} \quad (1)$$

Where m refers to the net evaporation rate calculated by subtracting evaporation under dark conditions from evaporation rate under one sun irradiation (1.5 kg m^{-2} h^{-1}), h_{lv} is the total liquid-vapor phase transition enthalpy (2260 kJ kg^{-1}), C_{opt} represents the optical concentration and q_i is the nominal solar radiation value of 1 kW m^{-2}.

A hydrophilic cellulose membrane was coated with **6′**$(OTf)_{12}$ to facilitate photothermal water evaporation performance, obtaining a typical double-layer evaporator. Note that the compound **6**$(OTf)_{12}$ was uniformly distributed on the cellulose membrane substrate (Fig. 7a). Interestingly, the studied supramolecular compounds exhibited remarkably different hydrophilicity values. Thus, we systematically measured the water contact angles of experimental samples and the cellulose film. The measured angles for the top samples and the bottom cellulose film were 85° and 5°, respectively (Fig. 7b). The superhydrophilic bottom of cellulose and the appropriate hydrophobicity of the upper portion of the sample **6**$(OTf)_{12}$ ensure efficient water supply while maintaining rapid vapor escape at the evaporation interface, ultimately resulting in the highest observed evaporation performance. The Janus membrane **6′**$(OTf)_{12}$ features unique porous properties and hydrophilicity to promote steam generation. The solar-thermal conversion of membranes composed of **5**$(OTf)_{12}$, **6**$(OTf)_{12}$ and **7**$(OTf)_{12}$ was investigated under 1 sun irradiation (1.0 kW m^{-2}). The surface temperature of the membranes rapidly increased upon light irradiation and reached 50.5 °C, 52.2 °C, and 51.5 °C, respectively (Fig. 7c, d). Subsequently, the evaporation performance was further evaluated using an indoor experimental setup (Fig. 7e). Owing to its Janus structure and solar thermal conversion, **6′**$(OTf)_{12}$ exhibited a higher evaporation rate (1.52 kg m^{-2} h^{-1}) than that of **5′**$(OTf)_{12}$ (0.77 kg m^{-2} h^{-1}) and **7′**$(OTf)_{12}$ (1.37 kg m^{-2} h^{-1}). Note that the evaporation rate recorded for **6′**$(OTf)_{12}$ is 3.45 times higher than that of bulk water (0.44 kg m^{-2} h^{-1}) (Fig. 7f). In addition, inductively coupled plasma mass spectrometry (ICP-MS) showed that the ion concentrations of Na^+, K^+, Mg^{2+}, Ca^{2+} in the collected fresh water after evaporation significantly decreased, fully meeting the drinking water standard indicated by the World Health Organization (WHO) (Fig. 7g). The membranes demonstrated remarkable durability under cyclic operation. Over 10 consecutive test cycles (6 h per cycle), they retained consistent evaporation rates and photothermal conversion performance (Fig. 7h). Particularly, when challenged with dye-contaminated wastewater, the evaporation performance showed merely a 8% reduction compared to pure water tests, and the sewage is transformed into clear and colorless water after being purified by our membrane evaporation, confirming their resistance to complex aqueous environments (Supplementary Figs. 80a, b). This combination of cycling stability and environmental tolerance positions these membranes as promising candidates for practical solar desalination applications. Compared to some porous materials such as MOF and COF reported in the literature, membrane **6′**$(OTf)_{12}$ is one of the best reported materials for photothermal water evaporation considering its solar-to-vapor efficiency and evaporation rate (Fig. 7i and Supplementary Table 9).

Discussion

In summary, three molecular-tweezer-like compounds, three interlocked cages, a tetranuclear macrocycle and a hexanuclear cage have been prepared and fully characterized. Remarkably, the interlocked cages have exhibited different photothermal conversion efficiencies, most likely due to their variable light quenching influence imparted by the half-sandwich units in the structure, as well as their internal π···π stacking interactions.

https://doi.org/10.1038/s41467-025-62787-7

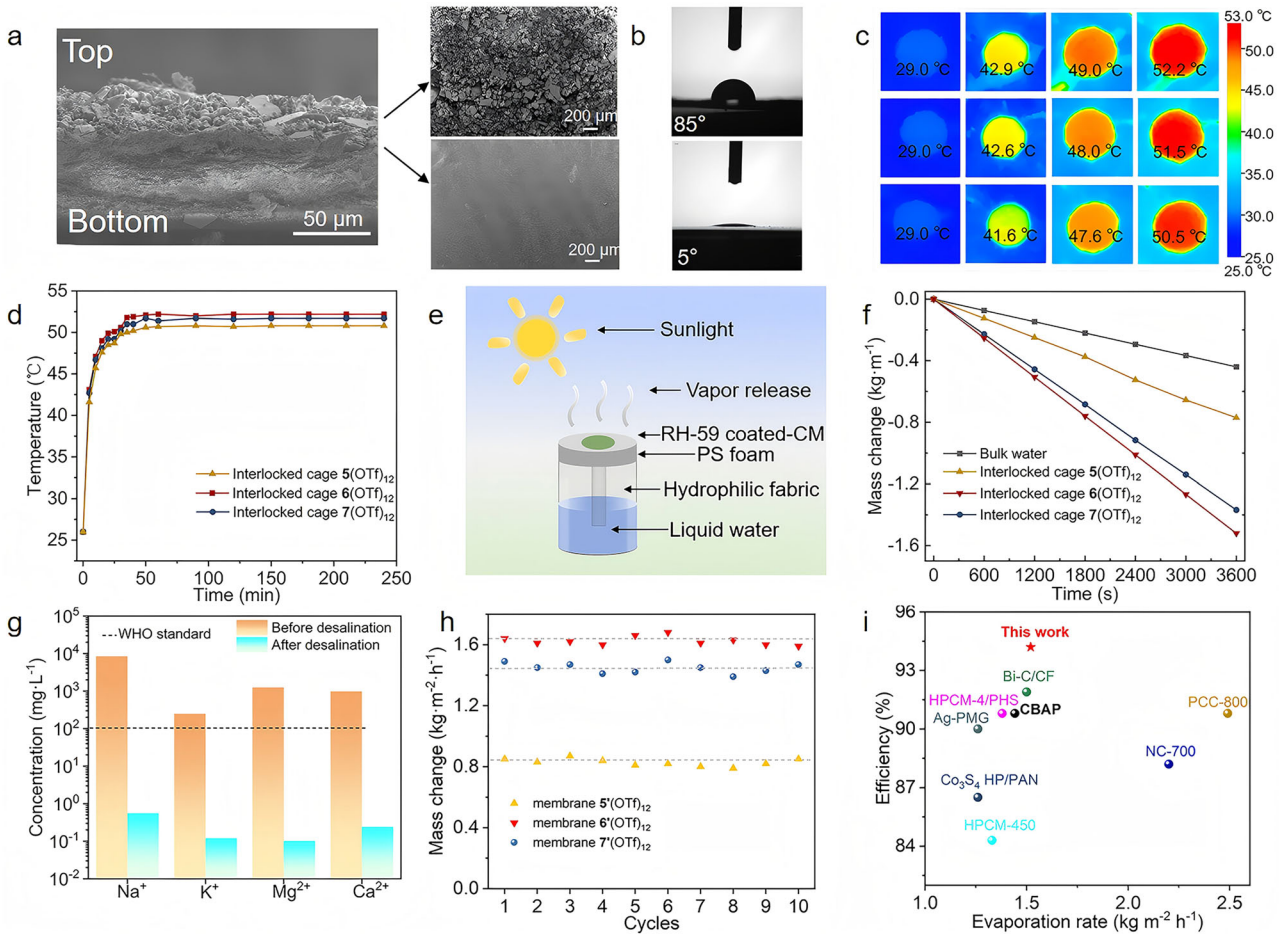

Fig. 7 | Seawater desalination experiment. a SEM images of the cross-section, top surface, bottom surface and **b** water contact angle of the top surface and bottom surface of the membrane **6'**$(OTf)_{12}$; **c** Thermal images and **d** time-dependent surface temperature of different membranes under 1 sun irradiation; **e** Schematic diagram of the interface water evaporation device (CM: cellulose membrane; PS: polystyrene); **f** Mass change of bulk water and different samples under 1 sun irradiation; **g** Ion concentration of water before and after desalination experiments; **h** Cycling performance of **5'**$(OTf)_{12}$, **6'**$(OTf)_{12}$ and **7'**$(OTf)_{12}$; **i** Comparison of water evaporation rates and efficiency of selected materials.

Recorded electron paramagnetic resonance (EPR) spectra provided a plausible explanation for their photothermal conversion performance. Based on the obtained experimental data, we have developed a series of membranes for the application in seawater desalination, by incorporating interlocked cages **5**$(OTf)_{12}$, **6**$(OTf)_{12}$, and **7**$(OTf)_{12}$ into a microcellular substrate, without the utilization of any additives. Membrane **6'**$(OTf)_{12}$ fully complies with hygienic standards, showed favorable stability, and demonstrated unique potential for water steam production in desalination processes. These results introduce a new promising application field for half-sandwich based materials.

Methods

Materials

All reagents and solvents were purchased from commercial sources and used as supplied unless otherwise mentioned. The starting materials $[Cp^*RhCl_2]_2$ (Cp^* = η5-pentamethylcyclopentadienyl)[52] was prepared by literature methods.

Synthesis of 1(OTf)$_8$, 2(OTf)$_8$ and 3(OTf)$_8$

In order to synthesize building blocks **E1**$(OTf)_2$, **E2**$(OTf)_2$ and **E3**$(OTf)_2$, added AgOTf (30.8 mg, 0.12 mmol) and $[Cp^*RhCl_2]_2$ (18.5 mg, 0.03 mmol) to 3 mL methanol. The container containing the mixture was sealed in tin foil and stirred at room temperature for 8 hours, then the white AgCl precipitate was filtered out by centrifuthe supernatant. Subsequently 2,5-dihydroxycyclohexa-2,5-diene-1,4-dione (16.8 mg, 0.03 mmol), 5,8-dihydroxynaphthalene-1,4-dione (5.7 mg, 0.03 mmol), 2,5-dibromo-3,6-dihydroxycyclohexa-2,5-diene-1,4-dione (8.93 mg, 0.03 mmol) and NaOH (2.4 mg, 0.06 mmol) were added to the above three filtrates respectively. Then the mixed solution was stirred at room temperature for 8 h to give a brown, green, and dark brown solution, building blocks **E1**$(OTf)_2$, **E2**$(OTf)_2$ and **E3**$(OTf)_2$ were obtained. Adding **L1** (9.6 mg, 0.03 mmol) to the solution, the mixture was stirred at room temperature for 8 h to give a dark earthy brown, dark green, and dark brown solution. Finally, the single crystals were grown by liquid diffusion, and the nonpolar solvent ether was added to the mixed solution of methanol and acetontrile. The product was recrystallized from a diethyl ether mixture to afford earthy brown block-shaped crystals **1**$(OTf)_8$, green needle-shaped crystals **2**$(OTf)_8$ and dark brown block-shaped crystals **3**$(OTf)_8$.

Characterization data for 1(OTf)$_8$ (Molecular-tweezer-like)

Total yield of crystals: 87.4%, ^1H NMR (500 MHz, CD_3OD, ppm, with respect to Cp*Rh): δ = 8.08 (d, 2H, J = 3.5 Hz, pyridyl-H_a), δ = 7.51 (d, 2H, J = 2.0 Hz, pyridyl-H_b), δ = 7.18 (d, 1H, J = 8.5 Hz, carbazolyl-H_d), δ = 6.78 (d, 1H, J = 7.0 Hz, carbazolyl-H_c), δ = 6.69 (s, 1H, carbazolyl-H_e), δ = 5.97 (s, 1H, benzoquinonyl-H_f), δ = 1.83 (s, 15H, Cp*-H_g); ESI-TOF-MS (m/z): $[\mathbf{1}(OTf)_8\text{-}3OTf]^{3+}$ calcd. for $C_{200}H_{188}O_{40}N_{12}F_{24}S_8Rh_8$, 1495.8121; found, 1495.8113 analysis (calcd., found for $C_{200}H_{188}O_{40}N_{12}F_{24}S_8Rh_8$): C (48.67,48.47), H (3.84, 3.74), N (3.41, 3.31).

Characterization data for 2(OTf)$_8$ (Molecular-tweezer-like)
Total yield of crystals: 86.7%. ^{1}H NMR (500 MHz, CD_3OD, ppm, with respect to Cp*Rh): δ = 8.30 (d, 2H, J = 6.0 Hz, pyridyl-H_a), δ = 7.51 (d, 2H, J = 6.5 Hz, pyridyl-H_b), δ = 7.72 (d, 1H, J = 4.5 Hz, carbazolyl-H_d), δ = 7.48 (s, 1H, carbazolyl-H_e), δ = 7.27 (d, 1H, J = 9.5 Hz, carbazolyl-H_c), δ = 6.44 (d, 2H, naphthyl-H_f), δ = 1.64 (s, 15H, Cp*-H_g); ^{13}C NMR (500 MHz, CD_3OD): δ 171.8, 171.4, 149.9, 149.4, 139.0, 121.9, 119.3, 111.6, 94.9, 56.1, 48.1, 47.9, 47.8, 47.6, 47.4, 47.2, 47.1, 15.9, 7.1, 6.9; ESI-TOF-MS (m/z): [**2**(OTf)$_8$-3OTf]$^{3+}$ calcd. for $C_{216}H_{196}O_{40}N_{12}F_{24}S_8Rh_8$, 1562.4996; found, 1562.4999; analysis (calcd., found for $C_{216}H_{196}O_{40}N_{12}F_{24}S_8Rh_8$): C (50.52,5032), H (3.85, 3.75), N (3.27, 3.17).

Characterization data for 3(OTf)$_8$ (Molecular-tweezer-like)
Total yield of crystals: 87.2%. ^{1}H NMR (500 MHz, CD_3OD, ppm, with respect to Cp*Rh): δ = 8.13 (d, 2H, J = 16.5 Hz, pyridyl-H_a), δ = 7.56 (d, 2H, J = 23.5 Hz, pyridyl-H_b), δ = 7.18 (d, 1H, J = 60.0 Hz, carbazolyl-H_d), δ = 6.77 (d, 1H, J = 35.0 Hz, carbazolyl-H_c), δ = 5.96 (s, 1H, carbazolyl-H_e), δ = 1.71 (s, 15H, Cp*-H_g). ^{13}C NMR (500 MHz, CD_3OD): δ 183.5, 183.4, 150.4, 141.3, 141.0, 124.1, 122.9, 122.5, 122.3, 121.6, 119.5, 118.0, 117.2, 110.8, 109.5, 102.0, 101.6, 95.6, 48.0, 47.9, 47.7, 47.6, 47.5, 47.3, 47.2, 7.6, 7.3; analysis (calcd., found for $C_{200}H_{180}O_{24}N_{12}Br_8F_{24}S_8Rh_8$): C (45.23,45.13), H (3.42, 3.32), N (3.17, 3.06).

Synthesis of 4(OTf)$_4$
The first step was to add AgOTf (30.8 mg, 0.12 mmol) and $[Cp^*RhCl_2]_2$ (18.5 mg, 0.03 mmol) to 3 mL methanol. The container containing the mixture was sealed in tin foil and stirred at room temperature for 8 hours, then the white AgCl precipitate was filtered out by centrifuthe supernatant. Subsequently, 2-(1H-benziMidazol-2-yl)-1H-benziMidazole (7.03 mg, 0.03 mmol) and NaOH (2.4 mg, 0.06 mmol) were added to the filtrate. Then the mixed solution was stirred at room temperature for 8 h to give a yellow solution, which contains building block **E4**(OTf)$_2$. Ligand **L1** (9.6 mg, 0.03 mmol) was added to the solution. The mixture was stirred at room temperature for 8 h to give a dark yellow solution. In the end, upon the addition of isopropyl ether, a dark yellow brown solid was precipitated and collected. The product was recrystallized from a diethyl ether mixture to afford dark yellow brown block-shaped crystals **4**(OTf)$_4$.

Characterization data for 4(OTf)$_4$ (Tetranuclear macrocycle)
^{1}H NMR (500 MHz, CD_3OD, ppm, with respect to Cp*Rh): δ = 8.21 (m, 1H, J = 9.0 Hz, phenyl-H_g), δ = 8.16 (m, 1H, J = 9.0 Hz, phenyl-H_f), δ = 7.75 (s, 1H, carbazolyl-H_e), δ = 7.68 (d, 2H, J = 5.5 Hz, pyridyl-H_a), δ = 7.66 (m, 1H, J = 9.0 Hz, phenyl-H_g), δ = 7.60 (m, 1H, J = 9.0 Hz, phenyl-H_f), δ = 7.22 (d, 2H, J = 5.5 Hz, pyridyl-H_a), δ = 7.04 (d, 1H, J = 8.5 Hz, carbazolyl-H_c), δ = 6.89 (d, 1H, J = 8.5 Hz, carbazolyl-H_d), δ = 1.94 (s, 15H, Cp*-H_h). ^{13}C NMR (500 MHz, CD_3OD): δ 157.0, 156.8, 151.4, 151.0, 144.1, 141.1, 124.9, 123.8, 123.5, 123.2, 122.9, 121.5, 119.4, 118.9, 115.9, 111.2, 97.2, 97.1, 48.0, 47.9, 47.7, 47.5, 47.4, 47.3, 47.1, 9.0; ESI-TOF-MS (m/z): [**4**(OTf)$_4$-2OTf]$^{2+}$ calcd. for $C_{116}H_{106}O_{12}N_{14}F_{12}S_4Rh_4$, 1178.7008; found, 1178.7021; analysis (calcd., found for $C_{116}H_{106}O_{12}N_{14}F_{12}S_4Rh_4$): C (52.22,52.12), H (4.46, 4.36), N (7.35, 7.25).

Synthesis of 5(OTf)$_{12}$, 6(OTf)$_{12}$ and 7(OTf)$_{12}$
Adding **L2** (9.49 mg, 0.02 mmol) to the solution of **E1**(OTf)$_2$, **E2**(OTf)$_2$ and **E3**(OTf)$_2$, the mixture was stirred at room temperature for 8 h to give a dark brown, dark green, and dark brown solution. Finally, the single crystals were grown by liquid diffusion, and the nonpolar solvent ether was added to the mixed solution of methanol and acetonitrile. The product was recrystallized from a diethyl ether mixture to afford earthy brown block-shaped crystals **5**(OTf)$_{12}$, dark green bar-shaped crystals **6**(OTf)$_{12}$ and dark brown block-shaped crystals **7**(OTf)$_{12}$.

Characterization data for 5(OTf)$_{12}$ (Interlocked cage)
Total yield of crystals: 87.5%, ^{1}H NMR (500 MHz, CD_3OD, ppm, with respect to Cp*Rh): δ = 8.71 (d, 2H, J = 5.5 Hz, pyridyl-H_a), δ = 8.54 (d, 2H, J = 5.5 Hz, pyridyl-H_i), δ = 8.14 (d, 2H, J = 5.0 Hz, pyridyl-H_b), δ = 8.13 (d, 2H, J = 5.5 Hz, pyridyl-H_f), δ = 8.02 (s, 1H, carbazolyl-H_e), δ = 7.95 (d, 2H, J = 5.5 Hz, carbazolyl-H_h), δ = 7.57 (d, 2H, J = 5.0 Hz, phenyl-H_g), δ = 7.24 (d, 1H, J = 9.0 Hz, carbazolyl-H_d), δ = 6.80 (d, 1H, J = 5.0 Hz, carbazolyl-H_c), δ = 6.04 (s, 1H, benzoquinonyl-H_k), δ = 1.85 (s, 15H, Cp*-H_j). ESI-TOF-MS (m/z): [**5**(OTf)$_{12}$-5OTf]$^{5+}$ calcd. for $C_{300}H_{280}O_{60}N_{16}F_{36}S_{12}Rh_{12}$, 2408.5520; found, 2408.5544; analysis (calcd., found for $C_{300}H_{280}O_{60}N_{16}F_{36}S_{12}Rh_{12}$): C (48.87,48.67), H (3.83, 3.73), N (3.04, 2.89).

Characterization data for 6(OTf)$_{12}$ (Interlocked cage)
Total yield of crystals: 89.1%. ^{1}H NMR (500 MHz, CD_3OD, ppm, with respect to Cp*Rh): δ = 8.75 (d, 2H, J = 5.0 Hz, pyridyl-H_a), δ = 8.56 (d, 2H, J = 7.0 Hz, pyridyl-H_i), δ = 8.15 (d, 2H, J = 1.5 Hz, pyridyl-H_b), δ = 7.94 (d, 2H, J = 9.0 Hz, carbazolyl-H_h), δ = 7.72 (d, 2H, J = 5.5 Hz, phenyl-H_f), δ = 6.44 (d, 2H, naphthyl -H_k), δ = 7.50 (d, 2H, J = 10.0 Hz, phenyl-H_g), δ = 6.63 (d, 1H, J = 8.0 Hz, carbazolyl-H_d), δ = 6.59 (s, 1H, carbazolyl-H_e), δ = 6.03 (d, 1H, J = 8.0 Hz, carbazolyl-H_c), δ = 6.04 (s, 1H, benzoquinonyl-H_k), δ = 1.77 (s, 15H, Cp*-H_j). ^{13}C NMR (500 MHz, CD_3OD): δ 171.7, 171.5, 171.2, 151.0, 150.8, 150.3, 150.0, 149.8, 139.9, 138.9, 126.2, 124.7, 124.4, 123.3, 123.2, 122.2, 116.8, 111.7, 111.6, 111.5, 95.2, 95.0, 94.9, 94.8, 94.7, 48.1, 48.0, 47.8, 47.6, 47.4, 47.3, 47.1; ESI-TOF-MS (m/z): [**6**(OTf)$_{12}$-3OTf]$^{3+}$ calcd. for $C_{324}H_{292}O_{60}N_{16}F_{36}S_{12}Rh_{12}$, 1325.5317; found, 1325.5325; analysis (calcd., found for $C_{324}H_{292}O_{60}N_{16}F_{36}S_{12}Rh_{12}$): C (49.77,49.64), H (3.91, 3.83), N (2.98, 2.87).

Characterization data for 7(OTf)$_{12}$ (Interlocked cage)
Total yield of crystals: 86.5%. ^{1}H NMR (500 MHz, CD_3OD, ppm, with respect to Cp*Rh): δ = 8.64 (d, 2H, J = 6.0 Hz, pyridyl-H_a), δ = 8.46 (d, 2H, J = 6.0 Hz, pyridyl-H_i), δ = 8.09 (d, 2H, J = 4.0 Hz, pyridyl-H_b), δ = 8.15 (d, 2H, J = 6.5 Hz, carbazolyl-H_h), δ = 8.04 (s, 1H, carbazolyl-H_e), δ = 7.88 (d, 2H, J = 8.0 Hz, phenyl-H_f), δ = 6.51 (d, 2H, J = 8.0 Hz, phenyl-H_g), δ = 6.26 (d, 1H, J = 8.5 Hz, carbazolyl-H_d), δ = 5.50 (d, 1H, J = 9.0 Hz, carbazolyl-H_c), δ = 1.93 (s, 15H, Cp*-H_j). ^{13}C NMR (500 MHz, CD_3OD): δ 177.8, 177.6, 177.5, 177.3, 151.6, 151.5, 151.2, 151.0, 150.8, 125.1, 124.7, 124.3, 124.2, 121.8, 119.3, 116.7, 96.6, 96.5, 96.3, 94.8, 48.1, 48.0, 47.8, 47.6, 47.3, 47.1, 8.2, 7.9, 7.8, 7.6, 7.5, 7.4, 7.3, 7.2; ESI-TOF-MS (m/z): [**7**(OTf)$_{12}$-5OTf]$^{5+}$ calcd. for $C_{300}H_{268}O_{60}N_{16}F_{36}S_{12}Br_{12}Rh_{12}$, 1514.7145; found, 1514.7102; analysis (calcd., found for $C_{300}H_{268}O_{60}N_{16}F_{36}S_{12}Br_{12}Rh_{12}$): C (43.31,43.21), H (3.25, 3.15), N (2.69, 2.59).H (3.42, 3.32), N (3.17, 3.06).

Synthesis of 8(OTf)$_6$
Adding **L2** (9.49 mg, 0.02 mmol) to the solution of **E4**(OTf)$_2$. The mixture was stirred at room temperature for 8 h to give a dark yellow solution. Then, upon the addition of diethyl ether, a dark yellow solid was precipitated and collected. The product was recrystallized from a diethyl ether mixture to afford compound **8**(OTf)$_6$.

Characterization data for 8(OTf)$_6$ (Hexanuclear cage)
^{1}H NMR (500 MHz, CD_3OD, ppm, with respect to Cp*Rh): δ = 8.23 (d, 2H, J = 5.5 Hz, pyridyl-H_a), δ = 8.16 (d, 2H, J = 6.5 Hz, pyridyl-H_i), δ = 8.02 (d, 2H, J = 5.5 Hz, phenyl-H_k), δ = 7.72 (d, 2H, J = 6.5 Hz, pyridyl-H_b), δ = 7.60 (d, 2H, J = 4.5 Hz, carbazolyl-H_h), δ = 7.58 (d, 2H, J = 5.5 Hz, phenyl-H_i), δ = 7.29 (s, 1H, carbazolyl-H_e), δ = 7.92 (d, 2H, J = 6.5 Hz, phenyl-H_f), δ = 7.31 (d, 2H, J = 6.5 Hz, phenyl-H_g), δ = 7.22 (d, 1H, J = 8.0 Hz, carbazolyl-H_d), δ = 7.11 (d, 1H, J = 8.5 Hz, carbazolyl-H_c), δ = 1.93 (s, 15H, Cp*-H_j). ^{13}C NMR (500 MHz, CD_3OD): δ 157.0, 156.8, 156.7, 151.7, 151.2, 150.4, 144.2, 144.1, 143.9, 139.8, 132.7, 127.2, 124.7, 124.7, 123.8, 123.6, 123.4, 123.2, 123.0, 122.7, 121.5, 119.5, 119.4, 115.9, 115.8, 110.5, 97.4, 97.2, 48.0, 47.9, 47.7, 47.6, 47.5, 47.3, 47.2, 9.1, 9.0; ESI-TOF-MS (m/z):

[**8**$(OTf)_6$-3OTf]$^{3+}$ calcd. For $C_{174}H_{158}N_{20}F_{18}S_6O_{18}Rh_6$, 1173.8641; found, 1173.8666; analysis (calcd., found for $C_{174}H_{158}N_{20}F_{18}S_6O_{18}Rh_6$): C (53.46,53.36), H (4.49, 4.39), N (6.85, 6.75).

Data availability

The X-ray crystallographic data reported in this article has been deposited at the Cambridge Crystallographic Data Centre (CCDC), under deposition number CCDC 2428612 (**1**$(OTf)_8$), 2400896 (**2**$(OTf)_8$), 2400898 (**3**$(OTf)_8$), 2400897 (**5**$(OTf)_{12}$), 2400895 (**6**$(OTf)_{12}$), 2445450 (**7**$(OTf)_{12}$). These data can be obtained free of charge from The Cambridge Crystallographic Data Centre via [www.ccdc.cam.ac.uk/data_request/cif]. The authors declare that all other data supporting the findings of this study are available within the paper and its supplementary information files. All data are available from the corresponding author upon request.

References

1. Kim, K. Mechanically interlocked molecules incorporating cucurbituril and their supramolecular assemblies. *Chem. Soc. Rev.* **31**, 96–107 (2002).
2. Zhang, Z. M. et al. Mechanically interlocked networks cross-linked by a molecular necklace. *Nat. Commun.* **13**, 1393 (2022).
3. Heard, A. W., Suárez, J. M. & Goldup, S. M. Controlling catalyst activity, chemoselectivity and stereoselectivity with the mechanical bond. *Nat. Rev. Chem.* **6**, 182–196 (2022).
4. Fyfe, M. C. T. & Stoddart, J. F. Interwoven supramolecular arrays via the noncovalent polymerization of pseudorotaxanes. *Coord. Chem. Rev.* **183**, 139–155 (1999).
5. Sauvage, J.-P. From chemical topology to molecular machines (nobel lecture). *Angew. Chem. Int. Ed.* **56**, 11080–11093 (2017).
6. Sawada, T. & Fujita, M. Folding and assembly of metal-linked peptidic nanostructures. *Chem* **6**, 1861–1876 (2020).
7. Saha, M. L., Yan, X. Z. & Stang, P. J. Photophysical properties of organoplatinum(II) compounds and derived self-assembled metallacycles and metallacages fluorescence and its applications. *Acc. Chem. Res.* **49**, 2527–2539 (2016).
8. Sun, Y., Chen, C. Y. & Stang, P. J. Soft materials with diverse suprastructures via the self-assembly of metal-organic complexes. *Acc. Chem. Res.* **52**, 802–817 (2019).
9. Greenfield, J. L. & Nitschke, J. R. Self-assembly of double-helical metallopolymers. *Acc. Chem. Res.* **55**, 391–401 (2022).
10. Guo, S. T., Cui, P. F., Liu, X. R. & Jin, G.-X. Synthesis of carborane-backbone metallacycles for highly selective capture of n-pentane. *J. Am. Chem. Soc.* **144**, 22221–22228 (2022).
11. Cui, P. F., Liu, X. R. & Jin, G.-X. Supramolecular architectures bearing half-sandwich iridium- or rhodium-based carboranes: design, synthesis, and applications. *J. Am. Chem. Soc.* **145**, 19440–19457 (2023).
12. Cui, Z., Mu, Q. S., Gao, X. & Jin, G.-X. Stereoselective construction of chiral linear [3]catenanes and [2]catenanes. *J. Am. Chem. Soc.* **145**, 725–731 (2023).
13. Dang, L. L. et al. Highly selective construction of unique cyclic [4] catenanes induced by multiple noncovalent interactions. *Angew. Chem. Int. Ed.* **64**, e202422444 (2025).
14. Colley, N. D. et al. Barnes topologically controlled syntheses of unimolecular oligo[n]catenanes. *ACS Cent. Sci.* **8**, 1672–1682 (2022).
15. Hung-Ng, A. W., Yee, C. C. & Au-Yeung, H. Y. Radial hetero[5] catenanes: peripheral isomer sequences of the interlocked macrocycles. *Angew. Chem. Int. Ed.* **58**, 17375–17382 (2019).
16. Ronson, T. K., Wang, Y., Baldridge, K., Siegel, J. S. & Nitschke, J. R. An s10-symmetric 5-fold interlocked [2]catenane. *J. Am. Chem. Soc.* **142**, 10267–10272 (2020).
17. Zhao, Y. et al. Highly selective synthesis and near-infrared photothermal response of heterometallic double trefoil knot and D-type [2]catenanes. *Sci. China Chem.* **68**, 1383–1391 (2025).
18. Shan, W. L., Gao, X., Lin, Y. J. & Jin, G.-X. Template-free self-assembly of molecular trefoil knots and double trefoil knots featuring Cp*Rh building blocks. *Chem. Eur. J.* **26**, 5093–5099 (2020).
19. Dang, L. L. et al. Triply interlocked [2]catenanes: rational synthesis, reversible conversion studies and unprecedented application in photothermal responsive elastomer. *Angew. Chem. Int. Ed.* **63**, e202406552 (2024).
20. Westcott, A., Fisher, J., Harding, L. P., Rizkallah, P. & Hardie, M. J. Self-assembly of a 3D triply interlocked chiral [2]catenane. *J. Am. Chem. Soc.* **130**, 2950–2951 (2008).
21. Yang, L. et al. Binding of anions in triply interlocked coordination catenanes and dynamic allostery for dehalogenation reactions. *Chem. Sci.* **9**, 1050–1057 (2018).
22. Yu, H. M. et al. Self-assembly of cluster-mediated 3D catenanes with size-specific recognition behavior. *J. Am. Chem. Soc.* **145**, 25103–25108 (2023).
23. Chen, T. et al. Self-assembly and photothermal conversion of metallarussian doll and metalla[2]catenanes induced via multiple stacking interactions. *J. Am. Chem. Soc.* **145**, 18036–18047 (2023).
24. Salazar, A. et al. Supramolecular subphthalocyanine cage as catalytic container for the functionalization of fullerenes in water. *Angew. Chem. Int. Ed.* **62**, e202311255 (2023).
25. Li, G. F. et al. Woven polymer networks via the topological transformation of a [2]catenane. *J. Am. Chem. Soc.* **142**, 14343–14349 (2020).
26. Zhang, H. N., Yu, W. B., Lin, Y. J. & Jin, G.-X. Stimuli-responsive topological transformation of a molecular borromean ring via controlled oxidation of thioether moieties. *Angew. Chem. Int. Ed.* **60**, 15466–15471 (2021).
27. Zhang, H. N., Yu, W. B., Lin, Y. J. & Jin, G.-X. Reversible structural transformation between a molecular solomon link and an unusual unsymmetrical trefoil knot. *J. Am. Chem. Soc.* **141**, 16057–16063 (2019).
28. Zhang, Y. W., Bai, S., Wang, Y. Y. & Han, Y. H. A strategy for the construction of triply interlocked organometallic cages by rational design of poly-nhc precursors. *J. Am. Chem. Soc.* **142**, 13614–13621 (2020).
29. Tamura, Y., Takezawa, H. & Fujita, M. A double-walled knotted cage for guest-adaptive molecular recognition. *J. Am. Chem. Soc.* **142**, 5504–5508 (2020).
30. Fujita, M., Fujita, N., Ogura, K. & Yamaguchi, K. Spontaneous assembly of ten components into two interlocked, identical coordination cages. *Nature* **400**, 52–55 (1999).
31. Sivalingam, V., Parbin, M., Krishnaswamy, S. & Chand, D. K. Cage-to-cage transformations in self-assembled coordination cages using "acid/base" or "guest binding-induced strain" as stimuli. *Angew. Chem. Int. Ed.* **63**, e202403711 (2024).
32. Feng, T., Li, X., Wang, Y. Y. & Han, Y. H. Backbone-directed self-assembly of interlocked molecular cyclic metalla[3]catenanes. *Angew. Chem. Int. Ed.* **59**, 13516–13520 (2020).
33. Singh, J. et al. The first quantitative synthesis of a closed three-link chain (6_1^3) using coordination and noncovalent interactions-driven self assembly. *J. Am. Chem. Soc.* **142**, 9327–9336 (2020).
34. Zhao, Y. et al. Size-controlled synthesis and near-infrared photothermal response of Cp*Rh-based metalla[2]catenanes and rectangular metallamacrocycles. *Chin. Chem. Lett.* **35**, 109298 (2024).
35. Tang, H., Zhang, H. N., Gao, X. & Jin, G.-X. The topological transformation of trefoil knots to solomon links via diels-alder click reaction. *J. Am. Chem. Soc.* **146**, 16020–16027 (2024).
36. Mu, Q. S., Gao, X., Cui, Z., Lin, Y. J. & Jin, G.-X. Selective construction of molecular Solomon links and figure-eight knots by fine-tuning unsymmetrical ligands. *Sci. China Chem.* **66**, 2885–2891 (2023).
37. Dang, L. L. et al. Selective synthesis and structural transformation of a 4-ravel containing four crossings and featuring Cp*Rh/Ir fragments. *Angew. Chem. Int. Ed.* **62**, e202301516 (2023).

38. Séjourné, S. et al. Chiral truxene-based self-assembled cages: triple interlocking and supramolecular chirogenesis. *Angew. Chem. Int. Ed.* **63**, e202400961 (2024).
39. Wang, Q. et al. Solution-phase dynamic assembly of permanently interlocked aryleneethynylene cages through alkyne metathesis. *Angew. Chem. Int. Ed.* **54**, 7550–7554 (2015).
40. Manawi, Y., Kochkodan, V., Hussein, M. A. & Hilal, N. Can carbon-based nanomaterials revolutionize membrane fabrication for water treatment and desalination? *Desalination* **391**, 69–88 (2016).
41. Xu, Z. H., Pang, Z. B., Yan, X. F. & Yu, L. M. Transition metal oxide electrode materials for capacitive deionization. *Chem. Eng. J.* **501**, 157257 (2024).
42. Jrad, A., Olson, M. A. & Trabolsi, A. Molecular design of covalent organic frameworks for seawater desalination: a state-of-the-art review. *Chem* **9**, 1413–1451 (2023).
43. Sheng, K., Tian, M. M., Zhu, J. Y., Zhang, Y. T. & Bruggen, B. V. When coordination polymers meet wood: from molecular design toward sustainable solar desalination. *ACS Nano* **17**, 15482–15491 (2023).
44. Gao, X. et al. Synthesis and near-infrared photothermal conversion of discrete supramolecular topologies featuring half-sandwich [Cp*Rh] units. *J. Am. Chem. Soc.* **143**, 17833–17842 (2021).
45. Xing, W. Q. et al. Thermo-responsive gold nanorod vesicles for combined NIR-II photothermal therapy and chemotherapy of solid tumors. *Acta Biomater.* **192**, 353–365 (2025).
46. Yue, F. et al. Efficient solar-driven: photothermal catalytic reduction of atmospheric CO_2 at the gas-solid interface by CuTCPP/MXene/TiO_2. *J. Colloid Interface Sci.* **677**, 758–770 (2025).
47. Wang, J., Du, P., Hsu, Y. I. & Uyama, H. Smart versatile hydrogels tailored by metal-phenolic coordinating carbon and polypyrrole for soft actuation, strain sensing and writing recognition. *Chem. Eng. J.* **493**, 152671 (2024).
48. Xie, Y. T. et al. Interfacial engineering of biocompatible nano-capsules for near-infrared-triggered drug release and photothermal therapy. *Adv. Sci.* **12**, 2410844 (2025).
49. Wang, C. B., Xu, K. Y., Shi, G. L. & Wei, D. Water skin effect and arched double-sided evaporation for boosting all-weather high salinity desalination. *Adv. Energy Mater.* **13**, 2300134 (2023).
50. Peng, Y. B. et al. Metal-organic framework composite photothermal membrane for removal of high-concentration volatile organic compounds from water via molecular sieving. *ACS Nano* **16**, 8329–8337 (2022).
51. Yan, X. L. et al. Superhydrophilic 2D covalent organic frameworks as broadband absorbers for efficient solar steam generation. *Angew. Chem. Int. Ed.* **134**, e202201900 (2022).
52. White, C., Yates, A. & Maitlis, P. M. (η^5-Pentamethylcyclopentadienyl) rhodium and -iridium compounds. *Inorg. Synth.* **29**, 228–234 (1992).

Acknowledgements

This work was supported by the National Science Foundation of China (22471113, 22171123, 22175094), Natural Science Foundation for Excellent Young Scholars of Henan Province (242300421139) and the Science and Technology Innovation Talent Program of University in Henan Province (25HASTIT001).

Author contributions

These authors contributed equally to this work: Ming-Yu Lu, Jian-Xin Yang, Ya-Ning Xu. M.-Y.L., J.-X.Y., and Y.-N.X. carried out the synthesis and characterization studies. Y.-H.C. analyzed the data. Y.Z. and F.A. solved the crystal structure. Y.-N.X. and X.-Q.W performed photothermal conversion studies. L.-L.D., Y.Z., D.T. and L.-F.M. directed the research. All of the authors contributed to the analysis of the results and the writing of the manuscript, with grant numbers [22471113] awarded to M.-Y.L., J.-X.Y. and L.-L.D., [22171123] to Y.-H.C. and L.-F.M., [22175094] to Y.-N.X. and D.T., [242300421139] to X.-Q.W. and Y.Z., and [25HASTIT001] to F.A.

Competing interests

The authors declare no competing interests.

Additional information

Supplementary information The online version contains supplementary material available at https://doi.org/10.1038/s41467-025-62787-7.

Correspondence and requests for materials should be addressed to Ying Zhao, Dan Tian or Li-Long Dang.

Peer review information *Nature Communications* thanks Guo-Xin Jin and the other, anonymous, reviewer(s) for their contribution to the peer review of this work. A peer review file is available.